

Band Narrowing and Mott Localization in Iron Oxychalcogenides $\text{La}_2\text{O}_2\text{Fe}_2\text{O}(\text{Se},\text{S})_2$

Jian-Xin Zhu,¹ Rong Yu,² Hangdong Wang,³ Liang L. Zhao,² M. D. Jones,⁴
Jianhui Dai,³ Elihu Abrahams,⁵ E. Morosan,² Minghu Fang,³ and Qimiao Si²

¹*Theoretical Division, Los Alamos National Laboratory, Los Alamos, New Mexico 87545, USA*

²*Department of Physics & Astronomy, Rice University, Houston, Texas 77005, USA*

³*Department of Physics, Zhejiang University, Hangzhou 310027, P. R. China*

⁴*University at Buffalo, SUNY, Buffalo, New York 14260, USA*

⁵*Center for Materials Theory, Rutgers University, Piscataway, New Jersey 08855, USA**

(Dated: February 13, 2022)

Bad metal properties have motivated a description of the parent iron pnictides as correlated metals on the verge of Mott localization. What has been unclear is whether interactions can push these and related compounds to the Mott insulating side of the phase diagram. Here we consider the iron oxychalcogenides $\text{La}_2\text{O}_2\text{Fe}_2\text{O}(\text{Se},\text{S})_2$, which contain an Fe square lattice with an expanded unit cell. We show theoretically that they contain enhanced correlation effects through band narrowing compared to LaOFeAs , and we provide experimental evidence that they are Mott insulators with moderate charge gaps. We also discuss the magnetic properties in terms of a Heisenberg model with frustrating J_1 - J_2 - J'_2 exchange interactions on a “doubled” checkerboard lattice.

PACS numbers: 71.10.Hf, 71.27.+a, 71.55.-i, 75.20.Hr

Introduction: Iron pnictides are the first non-copper-based compounds to exhibit high- T_c superconductivity [1, 2], and have therefore attracted considerable interest. How strong the electron correlations are in the parent iron pnictides is a subject of extensive current discussion. One viable description places these compounds at the boundary of itinerancy and Mott localization. The motivation for this incipient Mott picture comes from the observed bad metal properties [3, 4], and from first-principles calculations [5, 6] and related [7–9] considerations. Optical conductivity has in the meantime shown a sizable suppression of the Drude weight [10–12], as well as temperature-induced spectral-weight transfer going to energies of the eV range [11, 13, 14]. Inelastic neutron scattering experiments have provided complementary support. They have not only observed zone-boundary high-energy spin waves [15], but also shown [15, 16] that the total (ordered plus fluctuating) spin spectral weight is, for instance, about $1.2 \mu_B/\text{Fe}$ in CaFe_2As_2 . Such a large spin spectral weight implies that the low-energy spin degrees of freedom come from electronic excitations not only close to the Fermi energy but also far away from it. All these are defining properties of metals on the verge of Mott localization. To establish the incipient Mott picture, however, it is important to identify the Mott insulating part of the electronic phase diagram in the iron pnictides and related compounds.

Towards this end, we consider the iron oxychalcogenides $\text{La}_2\text{O}_2\text{Fe}_2\text{OSe}_2$ and $\text{La}_2\text{O}_2\text{Fe}_2\text{OS}_2$. These systems are built from stacking layered units La_2O_2 and $\text{Fe}_2\text{O}(\text{Se},\text{S})_2$. We will describe the Se case below, with the understanding that the S case is similar unless otherwise stated. Fig. 1 (left panel) shows the crystal structure with space group $I4/mmm$ as given in Ref. [17]. Each Fe_2OSe_2 layer contains a square lattice of Fe ions, and

this is the same as in an FeAs layer of LaOFeAs or an FeTe layer of the compound FeTe [18, 19]. In addition, Fe^{2+} is the nominal valence as in the latter materials. The Fe_2OSe_2 layer is unique in that the Fe ions in each plaquette are alternatively linked by an in-plane oxygen ion and by two selenium ions buckled on the two sides of the Fe square lattice. The inter-atomic distances are $d_{\text{Fe-Fe}} = 2.884 \text{ \AA}$, $d_{\text{Fe-O}} = 2.039 \text{ \AA}$, and $d_{\text{Fe-Se}} = 2.722 \text{ \AA}$.

An important observation is that Fe-square-lattice unit cell of $\text{La}_2\text{O}_2\text{Fe}_2\text{OSe}_2$ is slightly larger (by about 1%) than that of LaOFeAs and considerably larger than that of either FeTe (by over 6%) or FeSe (by over 8%) [18, 19]. This raises the possibility for a narrower bandwidth ($\propto t$) and, correspondingly, a larger strength of the normalized electron correlation, U/t . We have further been motivated by the indication of antiferromagnetic ordering (AFM) in the early work of Mayer and co-workers [17].

Band narrowing: We have determined the electronic structure using the WIEN2k linearized augmented plane wave method [20] based on density functional theory (DFT). A generalized gradient approximation (GGA) [21] was used to treat exchange and correlation.

In Fig. 2, we plot the projected density of states (DOS). In both compounds, we find that the 3d electrons on Fe contribute most to the DOS near the Fermi energy. The Fe d -electron DOS is mostly confined between -2 eV and 1.2 eV . This represents considerable narrowing of the Fe d -electron bands compared to LaFeAsO , where it occurs between -2.2 eV and 2 eV [22]. (There are also some differences between the two systems in the DFT-derived DOS near the Fermi energy, but the effective U/t primarily depends on the overall 3d-electron bandwidth.) The results for $\text{La}_2\text{O}_2\text{Fe}_2\text{OS}_2$ [dashed line of Fig. 2(a)] are similar. A comparable degree of 3d-electron band narrowing exists when the iron oxychalcogenides are com-

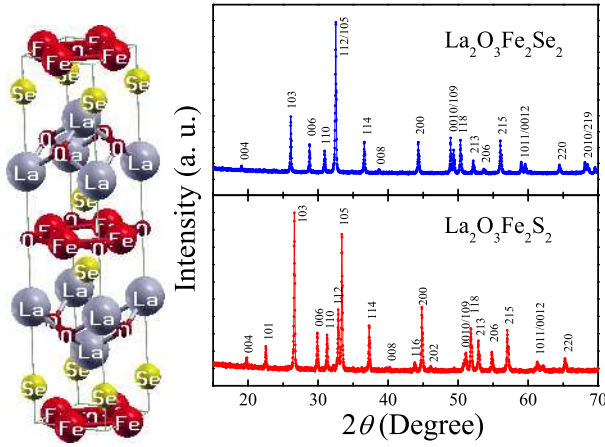


FIG. 1: (Color online) (Left panel) Crystal structure of $\text{La}_2\text{O}_2\text{Fe}_2\text{OSe}_2$; (Right panel) XRD patterns for the $\text{La}_2\text{O}_3\text{Fe}_2\text{Se}_2$ and $\text{La}_2\text{O}_3\text{Fe}_2\text{S}_2$ samples. The cell parameter values are $a = b = 4.085 \text{ \AA}$ and $c = 18.605 \text{ \AA}$ for $\text{La}_2\text{O}_3\text{Fe}_2\text{Se}_2$ and $a = b = 4.042 \text{ \AA}$ and $c = 17.929 \text{ \AA}$ for $\text{La}_2\text{O}_3\text{Fe}_2\text{S}_2$. Atomic positions in the unit cell of a paramagnetic state are as follows: La ($1/2, 1/2, 0.18445$), Fe ($0.5, 0, 0$), Se ($0, 0, 0.09669$), O1 ($1/2, 0, 1/4$), O2 ($1/2, 1/2, 0$).

pared to the iron chalcogenides FeTe and FeSe [23].

Mott insulating behavior: The narrower Fe 3d electronic bands point to enhanced correlation effects. To explore this, we have synthesized these materials following a similar procedure to that taken in Ref. [17] and measured their transport and magnetic properties. Polycrystalline samples with nominal composition $\text{La}_2\text{O}_3\text{Fe}_2\text{M}_2$ ($\text{M} = \text{S}$ or Se) were prepared by conventional solid state reaction using high purity La_2O_3 , Fe and S (or Se) powder as starting materials. The samples were characterized by powder X-ray diffraction (XRD) (right panel of Fig. 1) with Cu $K\alpha$ radiation ($\lambda = 1.5418 \text{ \AA}$) at room temperature.

The electrical resistivity as a function of temperature is shown in Fig. 3(a). For both $\text{M} = \text{Se}$ and $\text{M} = \text{S}$, the behavior is insulating with activation energy gaps [*cf.* inset of Fig. 3(a)] of about 0.19 eV and 0.24 eV, respectively. Figure 3(b) shows the temperature dependence of the bulk magnetic susceptibility $\chi(T)$, which exhibits a broad maximum around 120 K. The rapid decrease, at 93 K and 105 K, for $\text{M} = \text{Se}$ and $\text{M} = \text{S}$ respectively, is naturally ascribed to antiferromagnetic ordering in the Fe d -electron moments. At the lowest measured temperatures, $\chi(T)$ shows a small increase for $\text{La}_2\text{O}_3\text{Fe}_2\text{Se}_2$ but a small decrease for $\text{La}_2\text{O}_3\text{Fe}_2\text{S}_2$. This may be due to different impurities, whose amounts must be small as there is no trace of them in the XRD patterns.

The results provide evidence that both $\text{La}_2\text{O}_3\text{Fe}_2\text{Se}_2$ and $\text{La}_2\text{O}_3\text{Fe}_2\text{S}_2$ are Mott insulators, *i.e.* correlation-induced insulators with low energy spin excitations that order antiferromagnetically at low temperatures.

Magnetism: To investigate the Mott insulating state,

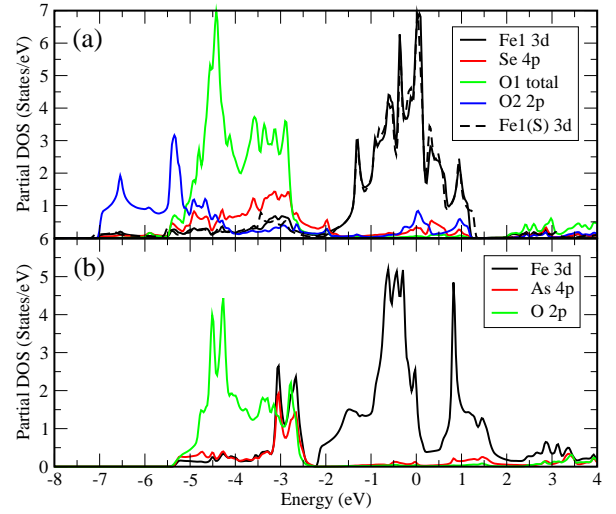


FIG. 2: (Color online) The partial DOS for paramagnetic $\text{La}_2\text{O}_2\text{Fe}_2\text{OSe}_2$ (a) and LaOFeAs (b). Also shown in Panel (a) is the Fe 3d partial DOS for $\text{La}_2\text{O}_2\text{Fe}_2\text{OS}_2$. In our DFT calculation, the energy threshold separating the localized and non-localized electronic states is chosen to be -6 Ryd . The muffin-tin radii are: $2.37 a_0$ (Bohr radius) for Lanthanum, $2.03 a_0$ for iron, $2.40 a_0$ for selenium, and $1.80 a_0$ for oxygen. The criterion for the number of plane waves is chosen to be $R_{\text{MT}}^{\text{min}} * K^{\text{max}} = 7$ and the number of k -points is $32 \times 32 \times 8$ for these paramagnetic-state calculations.

we extend our DFT calculations to the cases of magnetically ordered states using the GGA+ U method. We consider seven magnetic ground states, the building blocks for which are illustrated in Fig. 4. Each crystalline unit cell consists of two layers of Fe_2OSe_2 , whose coordinating geometry is rotated with respect to each other by 90° along the c -axis. Correspondingly, the seven spin states are formed with the spin alignment as follows: FM ((a)+(a)), AFM1 ((b)+(b)), AFM2 ((c)+(a)), AFM3 ((d)+(a)), AFM4 ((e)+(e)), AFM5 ((f)+(f)), and AFM6 ((e)+(e)'), where the notation ((spin1)+(spin2)) represents only the spin configuration rather than the underlying atomic coordination within each layer and the symbol (e)' represents the spin configuration obtained by rotating the configuration (e) in Fig. 4 by 90° . The energy differences between these spin ordered states for various on-site Hubbard interaction U are summarized in Table I. (None of the magnetically-ordered states at $U = 0$ has a gap in the DOS at the Fermi energy. Within GGA+ U , an insulating gap does develop for sufficiently large value of U , for some of the magnetic ordering patterns.) Based on considerations similar to the FeAs case [3, 26–28], we model the spin Hamiltonian in terms of nearest-neighbor (n.n.) exchange interaction (J_1) and the next-nearest-neighbor (n.n.n.) exchange interaction across an Fe-square plaquette with two buckled Se ions (J_2) and the n.n.n. interaction across an Fe-square plaquette containing the O-ion (J_2'). Even though the spin system is ex-

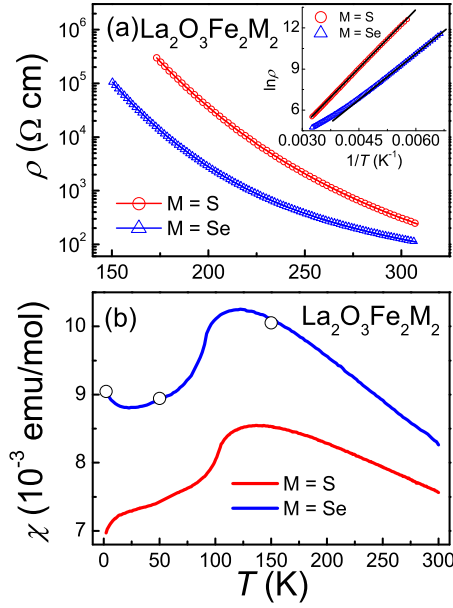


FIG. 3: (Color online) (a) The electrical resistivity (ρ) vs. temperature (T) for $\text{La}_2\text{O}_3\text{Fe}_2\text{S}_2$ and $\text{La}_2\text{O}_3\text{Fe}_2\text{Se}_2$. Inset: $\ln \rho$ vs. $1/T$; (b) The temperature dependence of susceptibility, χ , measured at 3 Tesla. The three open points, measured at 2 K, 50 K, and 150 K, respectively, are determined from the slope of the $M(H)$ curves.

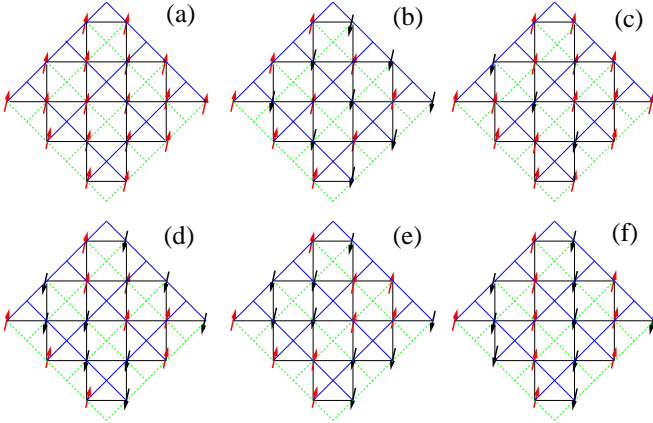


FIG. 4: (Color online) Schematic representation of the spin building blocks for the magnetically ordered states of $\text{La}_2\text{O}_2\text{Fe}_2\text{OSe}_2$. To be consistent with the effective model, only Fe atoms are shown. The arrows represent the spin orientation. The black solid, green dashed, and blue solid lines stand for J_1 , J_2 , and J'_2 spin exchange paths.

pected to be largely Heisenberg-type, the exchange parameters can be extracted by fitting the ground-state energies in terms of the Ising counterpart [24, 25]. We summarize the extracted exchange interactions in Table II.

We now turn to the effective J_1 - J_2 - J'_2 Heisenberg model defined on the two-dimensional doubled checkerboard lattice shown in Fig. 5(a). The classical Hamiltonian is $H = \sum_{\langle ij \rangle} J_{ij} \mathbf{S}_i \cdot \mathbf{S}_j$, where \mathbf{S}_i is a 3D vector

U (eV)	FM	AFM1	AFM2	AFM3	AFM4	AFM5	AFM6
0	0	226	39.7	-38.1	-10.7	45.5	-99.2
1.5	0	-164	-19.4	-69.6	-133	-209	-274
3.0	0	-241	-52.4	-90.4	-179	-237	-276
4.5	0	-216	-48.4	-74.2	-147	-188	-212

TABLE I: Relative energies ΔE (meV/unit cell) of the FM (ferromagnetic) and six AFM states of $\text{La}_2\text{O}_2\text{Fe}_2\text{OSe}_2$ obtained from GGA+ U calculations.

U (eV)	J_1/S^2	J_2/S^2	J'_2/S^2	σ
0	-3.53	2.10	9.23	139.5
1.5	2.53	-2.40	6.17	5.5
3.0	3.77	-1.11	4.79	1.27
4.5	3.38	-0.78	3.28	0.63

TABLE II: Values of spin exchange parameters J_1/S^2 , J_2/S^2 , J'_2/S^2 (meV) for $\text{La}_2\text{O}_2\text{Fe}_2\text{OSe}_2$ estimated from GGA+ U calculations. Positive (negative) J 's correspond to antiferromagnetic (ferromagnetic) exchange. The last column lists the “error bar” in energy (meV/unit cell): $\sigma = [\sum_{i=1}^N (\Delta E_M^{(i)} - \Delta E_M^{(i)})^2 / (N - 1)]^{1/2}$, where $N = 6$ and $\Delta E_M^{(i)}$ and $\Delta E_M^{(i)}$ are the relative ground-state energies in DFT and in the extracted effective spin models, respectively. σ is large for $U = 0$, but becomes relatively small for moderate values of U .

with magnitude S . To study the $T = 0$ phase diagram, for $J_1 > 0$, we rewrite the Hamiltonian via a summation over two sets of inter-penetrating plaquettes shown in Fig. 5(a):

$$H = -(J_2 + J'_2)NS^2 + \frac{1}{2} \sum_{m=A,B} \sum_{\square m} \{ J_{1m} (\sum_{i=1}^4 \mathbf{S}_i)^2 + J_{2m} [(\mathbf{S}_1 + \mathbf{S}_3)^2 + (\mathbf{S}_2 + \mathbf{S}_4)^2] \}, \quad (1)$$

where $J_{1A} = \alpha J_1$, $J_{1B} = (1 - \alpha)J_1$; $J_{2A(B)} = J_2(J'_2) - J_{1A(B)}$. Here $0 \leq \alpha \leq 1$ is a dummy control parameter [29], and N refers to the total number of plaquettes. The phase diagram is shown in Fig. 5(b). There are the Néel ordered AFM [for $0 < \alpha < 1$, $J_2 < \alpha J_1$, $J'_2 < (1 - \alpha)J_1$] and the collinear $(\pi, 0)/(0, \pi)$ ordered AFM [for $0 < \alpha < 1$, $J_2 > \alpha J_1$, $J'_2 > (1 - \alpha)J_1$] states. Unlike the square lattice J_1 - J_2 model, there also exists a plaquette $(\pi/2, \pi/2)$ AFM phase, which is stable for $J_2(J'_2) > J_1$ and $J'_2(J_2) < 0$. The transition between any two of the four ordered regions in the phase diagram is first order. Interestingly, we find that along the red solid boundaries in Fig. 5(b), the model loses any long-range magnetic order since the ground-state is infinitely degenerate. Along this boundary, $J_2 = J'_2 = 1/2$ corresponds to the maximally frustrated point of the J_1 - J_2 model, and $J_2(J'_2) = 0$ corresponds to the checkerboard AFM model. The phase diagram for $J_1 < 0$ can also be obtained by rotating all the spins in one sublattice of the underlying square lat-

tice (see Fig. 5(a)) $\mathbf{S}_i \rightarrow -\mathbf{S}_i$ and sending $J_1 \rightarrow -J_1$. It is similar to the one for $J_1 > 0$. The only difference is that the Néel ordered (π, π) phase is replaced by the FM phase ordered at $(0, 0)$.

The magnetic ground states expected from the exchange couplings given in Table II are marked in Fig. 5(b). For $U = 1.5$ eV and $U = 3.0$ eV, the ground state is the $(\pi/2, \pi/2)$ plaquette AFM state, while for larger U , i.e., $U = 4.5$ eV, the standard (π, π) Néel state is energetically favorable. Taking into account the stacking structure of the material, we see that these results are consistent with the DFT energies listed in Table I: the AFM6 state has the lowest energy for $U = 1.5$ eV and $U = 3.0$ eV, and the AFM1 state has the lowest energy for $U = 4.5$ eV.

To summarize, we studied the iron oxychalcogenides $\text{La}_2\text{O}_2\text{Fe}_2\text{O}(\text{Se}, \text{S})_2$, whose Fe-square lattice is expanded compared to that of the usually considered iron pnictides and chalcogenides. We have theoretically demonstrated that their Fe 3d-electron bands are narrower than the usual cases. The corresponding enhancement of correlation effects promotes the Mott insulating state, and this is demonstrated experimentally. Our demonstration of a Mott insulating phase in systems closely related to the iron pnictides extends the electronic behavior of these systems to a new regime. In addition, our results support the notion that the iron pnictides/chalcogenides possess intermediately strong electron correlations and are not too far away from Mott localization.

This work was supported by the National Nuclear Security Administration of the U.S. DOE at LANL under

Contract No. DE-AC52-06NA25396, the U.S. DOE Office of Science, and the LDRD Program at LANL (J.-X.Z.), the NSF Grant No. DMR-0706625, the Robert A. Welch Foundation Grant No. C-1411, and the W. M. Keck Foundation (R.Y. and Q.S.), the NSFC Grant No.10974175 and 10874147, the National Basic Research Program of China Grant No. 2009CB929104, and the PCSIRT of China Contract No. IRT0754 (H.W., J.D. and M.F.), and DoD MURI (L.L.Z. and E.M.). It was also supported in part by the Cyberinfrastructure for Computational Research funded by NSF under Grant CNS-0821727. J.-X.Z. thanks L. Cario for correspondence and the IT team at the Rice RCGS for help with computational resources.

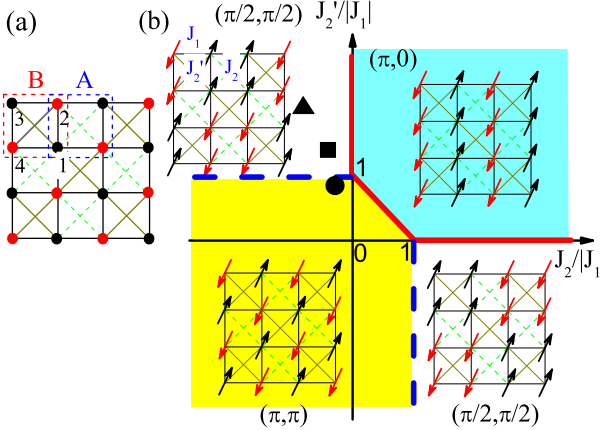


FIG. 5: (Color online) (a): The doubled checkerboard lattice for the Hamiltonian defined in Eq. (1). It consists of two sets of inter-penetrating plaquettes, indicated as blue (A) and red (B) dashed squares. It can be decomposed into two (red and black circle) sublattices. (b): The $T = 0$ phase diagram. The occupied symbols mark the ground states with exchange couplings listed in Table II, with $U = 1.5$ eV (triangle); $U = 3.0$ eV (square); $U = 4.5$ eV (circle).

* Current address: Department of Physics and Astronomy, University of California Los Angeles, Los Angeles, California 90095, USA.

- [1] Y. Kamihara *et al.*, J. Am. Chem. Soc. **130**, 3296 (2008).
- [2] Z. A. Ren *et al.*, Chin. Phys. Lett. **25**, 2215 (2008).
- [3] Q. Si and E. Abrahams, Phys. Rev. Lett. **101**, 076401 (2008).
- [4] Q. Si *et al.*, New J. Phys. **11**, 045001 (2009).
- [5] K. Haule *et al.*, Phys. Rev. Lett. **100**, 226402 (2008).
- [6] M. S. Laad *et al.*, Phys. Rev. B **79**, 024515 (2009).
- [7] M. Daghofer *et al.*, Phys. Rev. Lett. **101**, 237004 (2008).
- [8] C. Fang *et al.*, Phys. Rev. B **77**, 224509 (2008).
- [9] C. Xu *et al.*, Phys. Rev. B **78**, 020501(R) (2008).
- [10] M. M. Qazilbash *et al.*, Nat. Phys. **5**, 647 (2009).
- [11] W. Z. Hu *et al.*, Phys. Rev. Lett. **101**, 257005 (2008).
- [12] Q. Si, Nat. Phys. **5**, 629 (2009).
- [13] J. Yang *et al.*, Phys. Rev. Lett. **102**, 187003 (2009).
- [14] A. V. Boris *et al.*, Phys. Rev. Lett. **102**, 027001 (2009).
- [15] J. Zhao *et al.*, Nat. Phys. **5**, 555 (2009).
- [16] S. O. Diallo *et al.*, Phys. Rev. Lett. **102**, 187206 (2009).
- [17] J. M. Mayer *et al.*, Angew. Chem. Int. Ed. Engl. **31**, 1645 (1992).
- [18] M. H. Fang *et al.*, Phys. Rev. B **78**, 224503 (2008); W. Bao *et al.*, Phys. Rev. Lett. **102**, 247001 (2009).
- [19] F.-C. Hsu *et al.*, PNAS **105**, 14262 (2008).
- [20] P. Blaha *et al.*, *An Augmented Plane Wave + Local Orbitals Program for Calculating Crystal Properties* (K. Schwarz, Tech. Universität Wien, Austria, 2001).
- [21] J. P. Perdew *et al.*, Phys. Rev. Lett. **77**, 3865 (1996).
- [22] D. J. Singh and M.-H. Du, Phys. Rev. Lett. **100**, 237003 (2008).
- [23] A. Subedi *et al.*, Phys. Rev. B **78**, 134514 (2008).
- [24] D. Dai and M.-H. Whangbo, J. Chem. Phys. **118**, 29 (2003).
- [25] H. Kabbour *et al.*, J. Am. Chem. Soc. **130**, 8261 (2008).
- [26] T. Yildirim, Phys. Rev. Lett. **101**, 057010 (2008).
- [27] F. Ma *et al.*, Phys. Rev. B **78**, 224517 (2008).
- [28] Z. P. Yin *et al.*, Phys. Rev. Lett. **101**, 047001 (2008).
- [29] For any $0 \leq \alpha \leq 1$, Eq. (1) rewrites the J_1 - J_2 - J_2' Hamiltonian in the plaquette representation.